RESEARCH ARTICLE

DOI: 10.54392/irjmt2546

Asian Research Association

INTERNATIONAL RESEARCH JOURNAL OF
MULTIDISCIPLINARY TECHNOVATION

Taurolidine, a Sulfonic Amino Acid Derivative, Induces Apoptosis and Cytotoxicity against Cervical Cell Carcinoma an In Silico and in Vitro Approach

A. Mani [a], R. Elaiyaraja [a, *]

[a] Department of Microbiology, Shanmuga Industries Arts and Science College, Tiruvannamalai-606603, Tamil Nadu, India
* Corresponding Author Email: r.elaiyaraja@yahoo.in

DOI: https://doi.org/10.54392/irjmt2546
Received: 16-04-2025; Revised: 17-06-2025; Accepted: 02-07-2025; Published: 09-07-2025

Abstract: Taurolidine, a derivative of endogenous sulfonic amino acid taurine with a chemical formula of $C_7H_{16}N_4O_4S_2$ with antineoplastic, anti-inflammatory, cytotoxic, and antimicrobial characteristics, was subjected to *in silico* and *in vitro* studies. The fingerprint plots of the Hirshfeld surface analysis highlight that the O…H/H…O interaction makes a significant contribution with 57.4% of the total crystal packing. The biological interaction of taurolidine with antiapoptotic proteins Bcl-2 and Bcl-XL, characterized by binding energies of -5.54 and -6.92 kcal/mol, confirms its cytotoxic activity. The *in vitro* experiments were conducted against cervical carcinoma (SiHa) cells to confirm its antiproliferative activity. The MTT assay revealed that the cytotoxicity of taurolidine was observed in a dose-sensitive manner, with an IC_{50} (half maximal inhibitory concentration) at 204.1 µM, and induced cell cycle halt at the G0/G1 phase. The apoptotic characteristics of taurolidine-treated cells were measured using dual (AO/EtBr) and propidium iodide fluorescence staining. In addition, the mRNA expression analysis of proteins Bax and Bcl-2 confirms that taurolidine promotes apoptosis in cervical carcinoma cells.

Keywords: Taurolidine, Hirshfeld Surface Analysis, MTT Assay, Fluorescence Staining

---

1. Introduction

Cervical cancer (gynecological cancer) is the fourth major cause of carcinoma mortality in women worldwide. Cervical cancer is also known as the “disease of disparity” attribute of striking mortality within low, high, and middle-income countries [1]. With an annual incidence of 660,000, populations were newly diagnosed, and 350,000 mortalities worldwide in 2022 [2]. In India, it is estimated that 97,000 people were diagnosed with cervical cancer and 60,000 mortalities in 2018 [3]. Human papillomavirus is a significant cause of oncogenesis in women diagnosed with cervical cancer [4]. In addition, obesity, early menopause, smoking, lifestyle, and contamination with the human immunodeficiency virus also lead to an increase in the oncogenesis of cervical cancer [5]. The handling of patients with cervical cancer involves chemotherapy, radiation, surgery, hormonal therapy, and a combination of radiation and chemotherapy, depending on the patient history and stage of disease [6]. To reduce drug toxicity, chemoresistance, and therapeutic outcomes, the miRNA1284 combined with cisplatin has been delivered to cancer cells using a single nanocarrier liposome as a vector [7]. Taurolidine is a derivative of endogenous sulfonic amino acid taurine with a chemical formula of $C_7H_{16}N_4O_4S_2$ with antineoplastic, anti-inflammatory, cytotoxic, and antimicrobial properties [8]. Taurolidine downregulates the expression of transmembrane glycoprotein E-cadherin responsible for cell-cell adhesion *in-vivo* [9]. Taurolidine induces apoptosis and inhibits angiogenesis by down-regulation of anti-apoptotic proteins (Bcl-2 and Mcl1) and VEGF proteins [10]. In addition, taurolidine is also combined with antibiotics to treat peritonitis and endotoxic shocks. At a concentration of 100, 250, and 1000µg taurolidine induces cytotoxicity (apoptosis and necrosis) against five different neoplastic human cancer cell lines [11].

Due to its unique bioactive characteristics, taurolidine has gained significant attention in industrial and pharmaceutical applications. An earlier study used the DFT method to decipher its spectroscopic characteristics [12]. The antiproliferative properties of taurolidine against gastric cancer, glioblastoma, colon carcinoma, mesothelioma, and squamous cell carcinoma have been reported earlier [13-15]. However, the cytotoxic characteristics of taurolidine against human cervical cancer are still under scrutiny. Hence, our present investigation is to provide a detailed *in-vitro* cytotoxic activity of taurolidine against human cervical carcinoma.

2. Materials and Methods

2.1. Computational Details

The CIF (Crystallographic Information File) of taurolidine was downloaded from the Cambridge Crystallographic Data Centre (CCDC) [16]. The Hirshfield surface prediction including d_{norm}, Shape index, Curvedness and 2D fingerprint plots of taurolidine was forecast using the Crystal Explorer 21 program [17]. In addition, the binding affinity of taurolidine against antiapoptotic protein Bcl-2 and Bcl-XL was performed using AutoDock software [18]. The 2D and 3D outputs were emphasized using LigPlot and PyMol programs [19, 20]. The topological RDG and NCI approaches were calculated using MultiWfn software [21]. In addition, the Ramachandran plots for target proteins were plotted using PDBsum [22].

2.2. Cell Culture and Taurolidine Treatment

The human cervical carcinoma SiHa cells were acquired from NCCS (National Centre for Cell Science) Pune. The carcinoma cells were grown in a DMEM (Dulbecco`s Modified Eagle Medium) medium enhanced with 10% FBS (Fetal Bovine Serum) and cultures at 37ºC with 5% CO_2.

2.3. MTT assay

The antiproliferative effect of taurolidine was performed using MTT assay [23]. The untreated SiHa cell cline was planted in 96-well plates with a population of 1×10^5 cells/well. The cells are induced with various concentrations of taurolidine within 5 to 300 µM. Following the treatment, the cells are incubated with 10µl of MTT for 4 hours. After the incubation, the existing medium was discarded, and 100 µL of DMSO was supplemented to soluble the formazan crystals and read at 570nm.

2.4. Propidium Iodide Staining

The morphological changes of the nucleus after the treatment with taurolidine were measured using propidium iodide (PI) staining, which was made using the methodology proposed by Chandramohan *et al.,* [24]. SiHa cells were grown in 6-well plates at a population of 5×104 with sterile coverslips in each well. The SiHa cells are allowed to incubate at 37°C using CO2 incubator for 24h to reach the confluence of eighty percent. After incubation, the cells were induced with taurolidine at a dosage of 204.1 µM for 24h. The cells treated with taurolidine the DMEM medium was removed and washed the cells with PBS solution. The morphological characteristics of nucleus in taurolidine treated cells were measured using fluorescence microscope.

2.5. Acridine Orange/EtBr Staining

The early apoptotic, apoptotic and necrotic characteristics of taurolidine treated cells were examined using dual staining according to the methodology proposed by Gohel *et al.,* [25]. The cells cultured in DMEM medium was incubated for 24h at 37ºC using CO2 incubator. After the cells treated with taurolidine using IC50 concentration for 24h. Then the cells were stained with AO/EtBr solution and observed under a fluorescence microscope.

2.6. Cell Cycle Analysis

The carcinoma cells cultured in sterile plates and then treated with IC_{50} concentration of taurolidine for 24h. After treatment the cells were centrifuged and fixed in ice-cold 70% ethanol solution for overnight. After incubation the cells stained with PI solution for 30 min at room temperature. After the distribution of cell cycle was analyzed using flow cytometer.

2.7. Quantitative RT-PCR Analysis

To quantify the expression of anti-apoptotic genes, the total RNA was extracted from taurolidine-treated cells using methodology detailed by Chomczynski *et al.,* [26]. The primers used to convert RNA to cDNA for Bax (forward 5`-TGCTTCAGGGTTTCATCCAG-3`, reverse 5`-GGCGGCAATCATCCTCTG-3`) and Bcl-2 (forward 5`-AGATGTCCAGCCAGCTGCACCTGAC-3`, reverse 5'-AGATAGGCACCCAGGGTGATGCAAGCT-3`) with an annealing temperature of 55.5°C and 57.5°C, respectively. Glyceraldehyde-3-phosphate dehydrogenase an enzyme used as intrinsic control to confirm the equal loading. in addition, all the PCR measurements were measured in triplicate in different replicates.

3. Results and Discussions

3.1. Hirshfeld Surface Analysis

The intramolecular interactions of taurolidine with respect to crystal structure were depicted in Figure. 1 and tabulated in Table 1. The Crystallographic Information File (CIF) of taurolidine was obtained from the Cambridge Crystallographic Data Centre (CCDC) and confirmed with single-crystal X-ray diffraction analysis, with a high resolution of 0.755 Å [16]. The d_i, d_e, and d_{norm} of taurolidine were calculated between 0.8175 to 2.6288, 0.8174 to 2.6207, and -0.4896 to 1.4858, respectively. The surface maps with red, white, and blue pigments emphasize the solid intermolecular interactions with shorter, equal, and longer to the sum of Van der Walls radii [27, 28]. The 2D fingerprint plot on the crystal structure of taurolidine reveals that oxygen-hydrogen interaction plays a significant contribution with

57.4% of the total crystal packing. A clear spike noticed in the fingerprint plot for O…H/H…O reveals the hydrogen bonding between the oxygen atom in sulfonyl groups and hydrogen atoms in the methylene groups with a bond distance of 2.341 and 2.806Å. The second solid contribution was simulated within H…H interaction with 35.6%. In addition, N…H/H…N and N…O/O…N shows minor contributions of 6.8 and 0.2%, respectively.

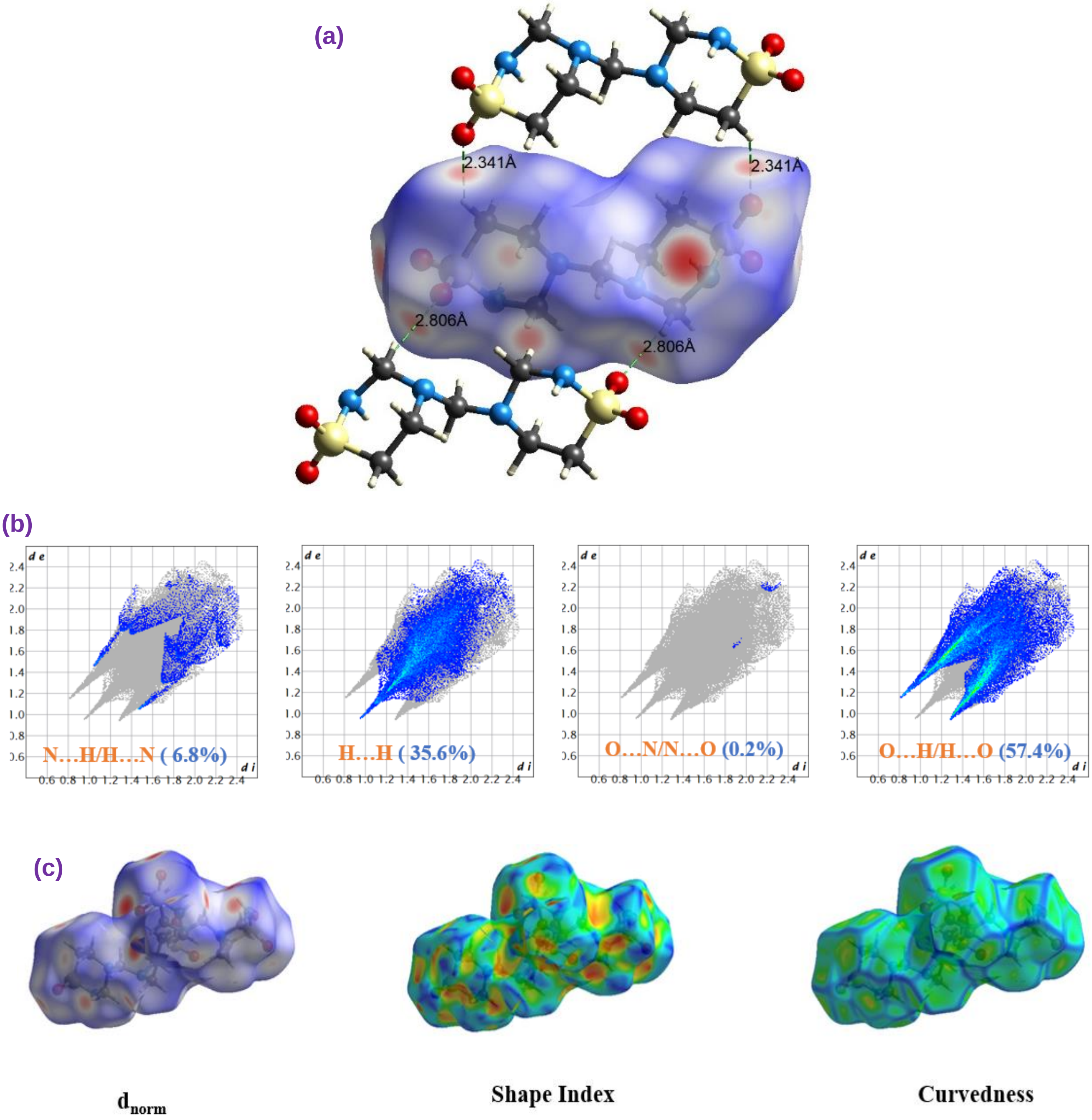

Figure. 1 (a). The 3D d_{norm} Hirshfeld surface inter-contacts of taurolidine, **(b).** Two-dimensional fingerprint plots of taurolidine, **(c).** Hirshfeld surfaces for taurolidine

Table 1. Relative contributions (%), intermolecular interactions of the Hirshfeld surface zone of taurolidine

Major contributions		**Minor contributions**	
H…H	O…H/H…O	O…N/N…O	N…H/H…N
35.6	57.4	0.2	6.8

3.2. RDG and NCI

The weak interactions (steric repulsion, polar bondings, and Van der Waals interactions) within the crystal packing of taurolidine have been emphasized using NCI and RDG topological analysis [29]. The calculated NCI isosurface and RDG scattered polts of taurolidine were depicted in Figure. 2. The blue, red, and green spikes in the RDG scattered plot highlight the polar bondings, steric repulsion, and van der Waals interactions. From the present investigation, a solid green and red spikes with the absence of blue spikes were noticed in the RDG scattered plot confirming that steric repulsion and van der Waals interactions play a crucial role in stabilizing the crystal packing of taurolidine. In contrast, the isosurface NCI plot highlights the red pigment simulated within the ring structures and methylene (CH_2) groups emphasize the steric repulsions and green pigments were observed between the sulfonyl (SO_2) and methylene (CH_2) groups. These theoretical findings from NCI and RDG suggest that Van der Waals interactions and steric repulsions significantly influence the molecular structure of taurolidine.

These noncovalent interactions demonstrate that the molecular structure of taurolidine adopts a rigid and bioactive molecular conformation. The steric repulsion clouded around the key functional groups prevents taurolidine's metabolic and enzymatic degradation, thereby enhancing the structural framework in the cellular environment. In addition, the moderate Van der Waals interactions between sulfonyl and methylene groups contribute to conformational stability and reduce the nonspecific interactions with the cellular components. The increased selectivity is crucial in antibacterial, antiproliferative characteristics and its ability to modulate inflammatory response.

3.3. Ramachandran plot

The Ramachandran plots for the target proteins (PDB.ID 6O0K and 2YXJ) were emphasized using the PDBsum bioinformatics tool [22]. The dihedral angles, including phi (ϕ) and psi (ψ) have been calculated between -180 to +180° to highlight the conformational zones within the target proteins. The graphical representation of the Ramachandran plot for the target proteins is depicted in Figure. 3. In the colored plot, the yellow, orange, red, and white regions correspond to allowed, additional allowed, most favorable, and disallowed conformations, respectively. In this investigation, the amino acid residues of the target protein are simulated within the most favorable and marginally present in the allowed regions. In addition, an increased population of amino acids fell at the -a region highlight left-handed alpha-helix structure, while residues in the B region correspond to β-sheets structures. These findings suggest that the target proteins are structurally stable.

3.4. Molecular Docking

Molecular docking is a theoretical tool used in drug discovery and synthesis to emphasize the interactions (polar and nonpolar) and binding affinities of target proteins and ligands [30-32]. The molecular docking was made to highlight the inhibitory characteristic of taurolidine against proteins to suppress apoptosis. The 3D native structure of proteins 6O0K and 2YXJ was confirmed with X-ray diffraction with a resolution of 1.62 and 2.20Å, respectively. The ligand taurolidine was optimized with GaussView 6.0 and kept in PDB format. In the present work, taurolidine forms three hydrogen bonds with Bcl-2 protein between the carboxyl group (COOH) of aspartic acid 31 and a nitrogen atom in taurolidine, with bond distances of 2.85 and 4.93 Å. In contrast, aspartic acid 34 is linked to a nitrogen atom with a bond distance of 4.98 Å. Additionally, the nitrogen atom of histidine 20 is linked to the oxygen atom in the sulfonyl (SO_2) group of taurolidine with a bond distance of 2.71 Å.

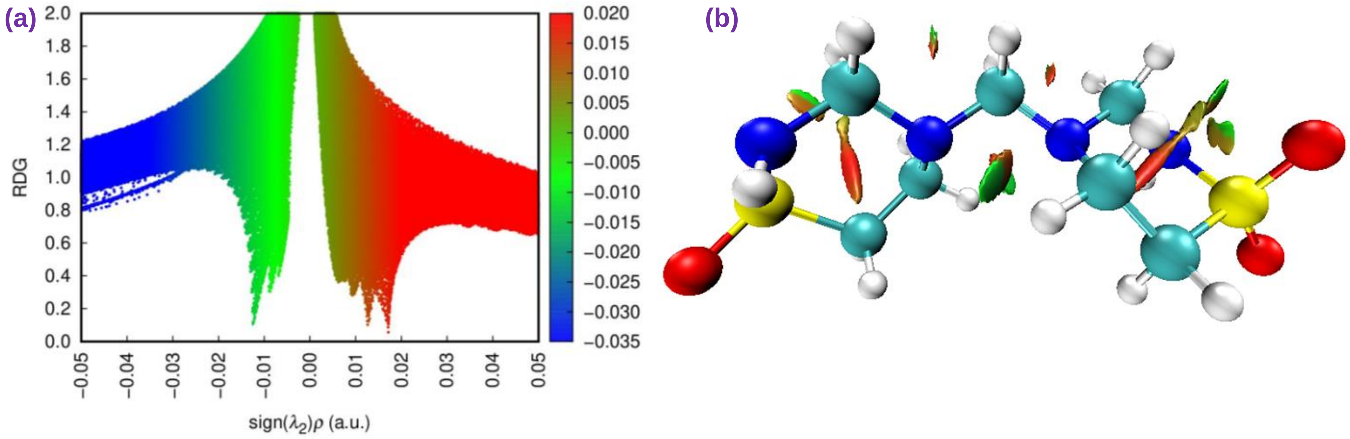

Figure 2 (a). Scatter RDG graph, and **(b)** isosurface NCI diagram of taurolidine

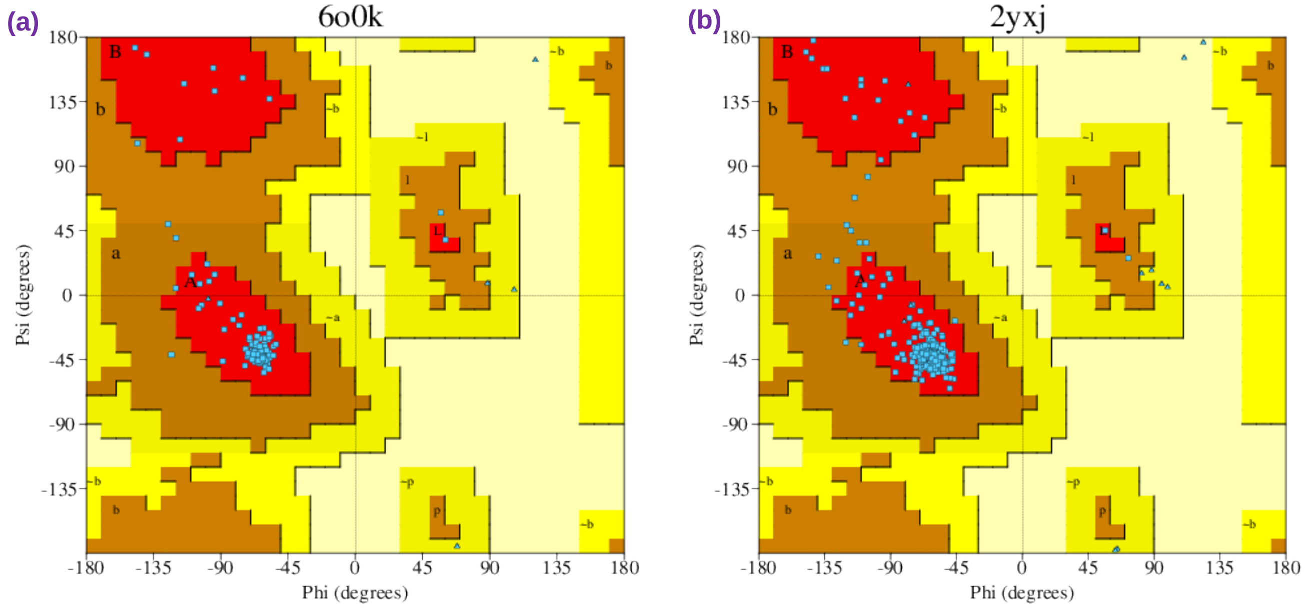

Figure 3. Ramachandran plots of target proteins 6O0K **(b)** 2YXJ

Table 2. Molecular interaction of taurolidine against 6O0K and 2YXJ proteins

Protein	PDB ID	No. of hydrogen bonding	Amino acids	Bond length (Å)	Hydrophobic interaction	Docking score
Bcl-2	600K	5	Tryptophan 30 Histidine 20 Aspartic acid 31 Aspartic acid 34	2.64 2.71 2.85, 4.93 4.98	Tyrosine 28 Serine 24 Glutamic acid 29	-5.54
Bcl-XL	2YXJ	6	Arginine 165 Serine 164 Glutamine 160 Serine 23 Serine 25	5.84 3.45 5.48 3.12, 2.84 3.91	Tryptophan 24 Tyrosine 22 Valine 163	-6.92

Table 3. Comparative binding affinity of taurolidine and standard inhibitors with target proteins

Ligands	Target protein	PDB ID	Binding affinity (kcal/mol)
Taurolidine	Bcl-XL	2YXJ	-6.92
ABT-737 (known inhibitor)	Bcl-XL	2YXJ	-10.05
Taurolidine	Bcl-2	6O0K	-5.54
Obatoclax (known inhibitor)	Bcl-2	6O0K	-7.47

The third hydrogen bond was simulated between the amino (NH_2) nitrogen of tryptophan 30 and the electronegative nitrogen of taurolidine with a bond distance of 2.64 Å. In addition, amino acids tyrosine 28, glutamic acid 29, and aspartic acid 34 create hydrophobic interactions with taurolidine with a binding energy of -5.54 kcal/mol. In contrast, taurolidine exhibits significant hydrophobic interactions with amino acids tryptophan 24, tyrosine 22, and valine 163 of Bcl-XL. The polar interactions were observed between oxygen and nitrogen atoms of taurolidine with amino acids arginine 165, serine 164, glutamine 160, serine 23, and serine 25, with bond distances of 5.84, 3.45, 5.48, 3.12, 2.84 and 3.91 Å, respectively, with a binding affinity of -6.92 kcal/mol.

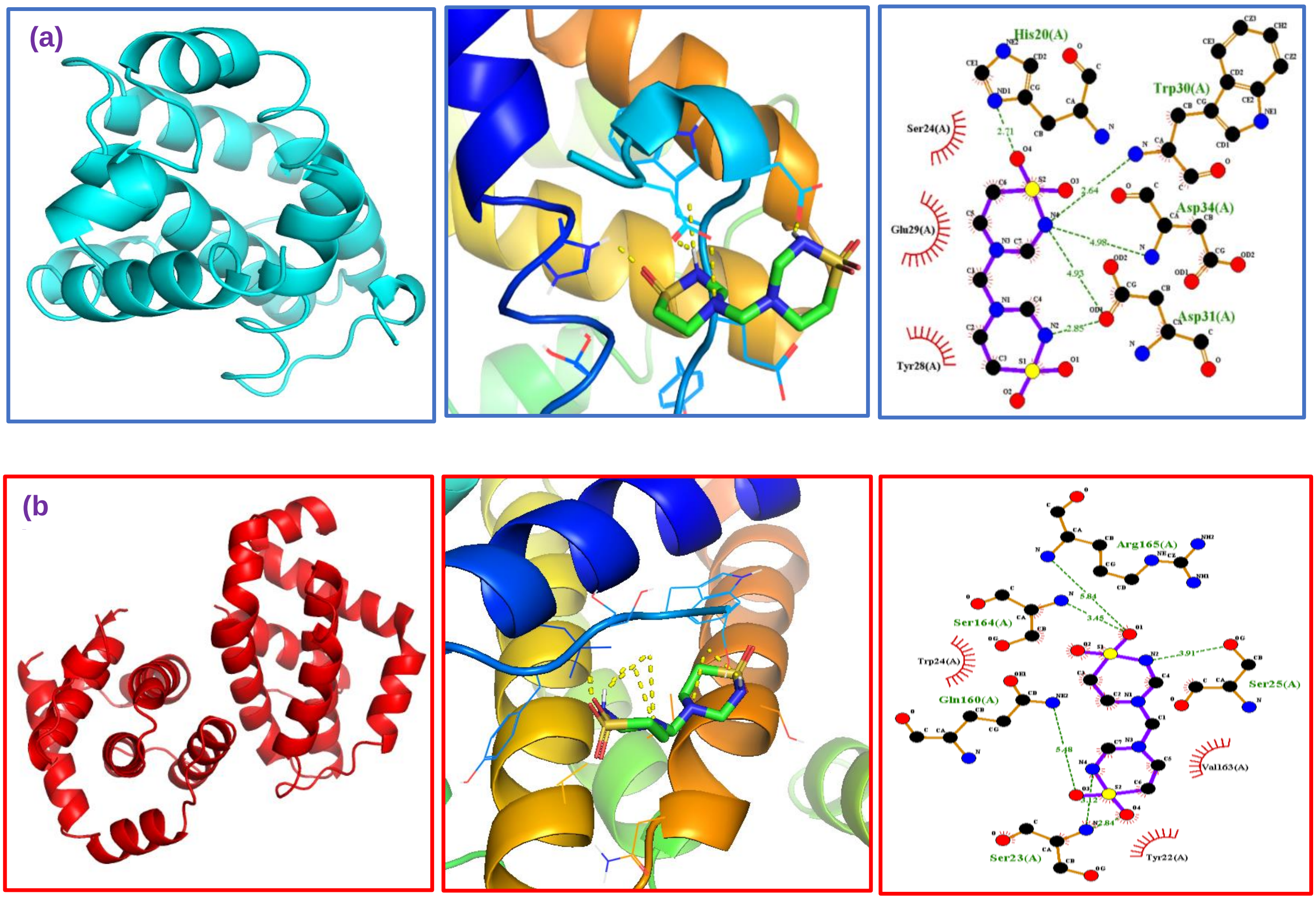

Figure 4(a). The native, 3D and 2D interaction view of taurolidine against 6O0k protein, **Figure 4(b).** The native, 3D and 2D interaction view of taurolidine against 2YKJ protein

These findings highlight the antagonist property of taurolidine against target proteins to suppress the apoptotic signals. The 3D and 2D ligand-protein interactions and the conforming binding energies are presented in Figure. 4 and Tables 2 and 3, respectively. From Table 3, taurolidine demonstrates moderate bonding affinity compared to known inhibitors, which exhibits significant bonding affinity with -10.05 and -7.47 kcal/mol for Bcl-XL and Bcl-2, respectively. However, due to its low cytotoxicity and favorable pharmacological profile, taurolidine is advantageous over conventional chemotherapeutic agents with significant side effects.

3.5. Cell morphological and proliferation assay

The cytotoxic characteristics of taurolidine against cervical cancer cell line SiHa cells were emphasized using MTT assay. The cells were induced with taurolidine at concentrations (5, 25, 50, 75, 150, and 300 µM) for 24hrs. The results highlight that the growth inhibition of taurolidine was observed in a dose-sensitive manner compared with the control. In addition, the percentage of cell death increased in the presence of taurolidine with an IC_{50} (half maximal inhibitory concentration) at 204.1 µM. The ratio of cell death was calculated by comparing the percentage of viable cells in control with viable cells treated with taurolidine and the corresponding graphical representation was shown in Figure 5. The morphology of cells treated with taurolidine (5, 25, 50, 75, 150, and 300 µM) concentrations and control were depicted in Table 4 and Fig. 6 using light microscopy.

3.6. Taurolidine promotes cell cycle arrest in SiHa cells

The SiHa cells were exposed to taurolidine at a concentration of 204.1 µM for 24hrs, the treated cells were subjected to flow cytometric analysis to measure the population of cells in each phase of the cell cycle. In the present investigation, after 24hrs of taurolidine administration, the concentration of cells increased in the G0/G1 phase with 74.96% compared to control with 59.08% and concomitant reduction in the concentration of cells at S and G2/M phases of the cell cycle. The percentage of cell cycle arrest in taurolidine-treated and control cells were depicted in Figure. 7 and Table 5.

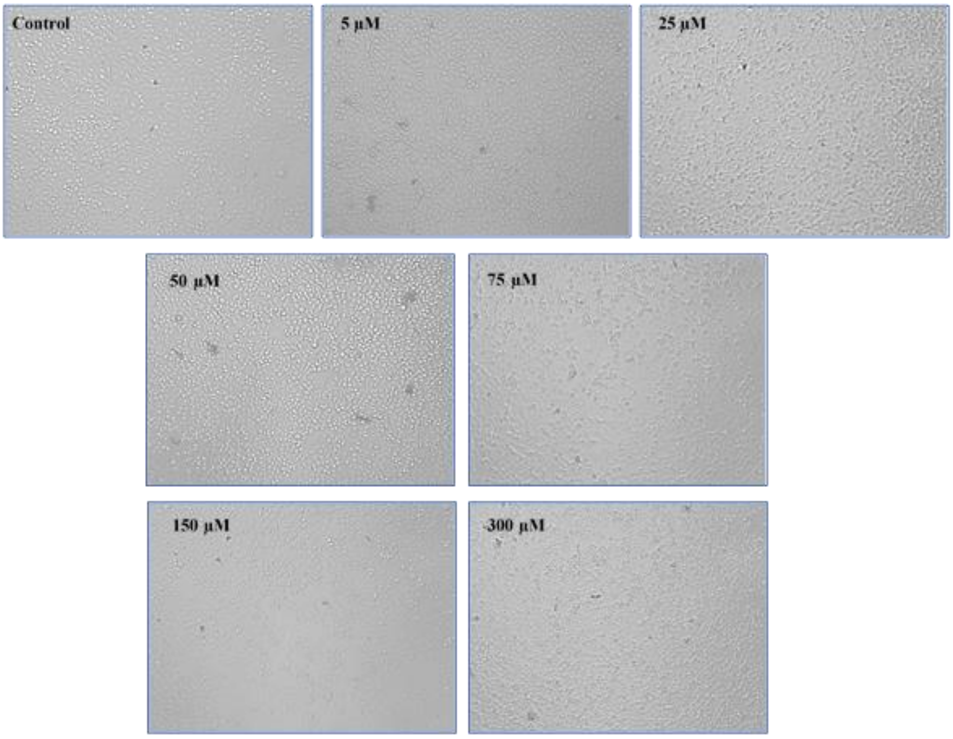

Figure 5. Morphology of control (untreated) and taurolidine-treated cells with different concentrations (5, 25, 50, 75, 150, and 300 µM) was observed using inverted light microscope.

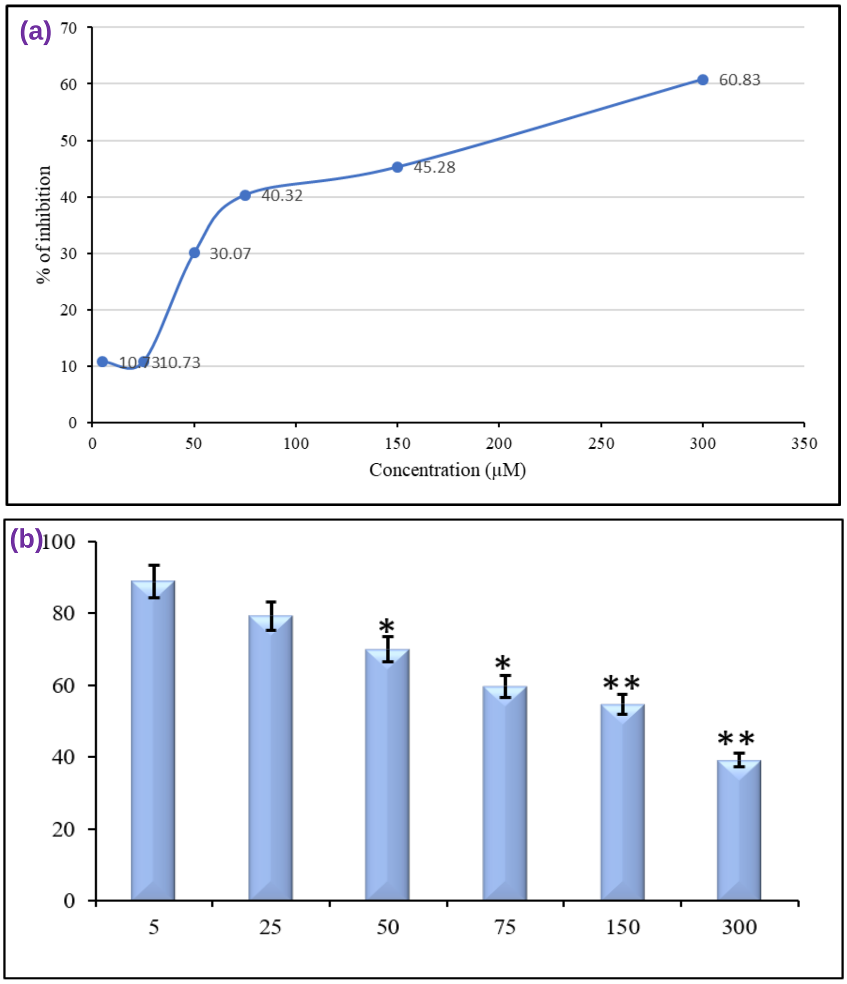

Figure 6. Cytotoxic effect of taurolidine in cultured SiHa cells. The cells were treated with taurolidine at various concentrations (5, 10, 25, 50, 100, 200, and 300 µM) for 24 h, and the cytotoxicity was assessed using the MTT assay a) sigmoidal curve and b) bar diagram. Outputs are presented as (mean ± SD) n=3. The statistical significance was made with control and significance were presented as * $p<0.05$ and ** $p<0.01$.

Table 4. Quantitative cytotoxicity measurement of taurolidine in hepatocellular carcinoma (Mean ±SD, n=3)

Concentration (μM)	Absorbance (Mean ± SD)	T/C Ratio	% of viability	% of inhibition
Control	1.370 ± 0.096	1.000	100.00	0.00
5	1.223 ± 0.179	0.893	89.27	10.73
25	1.217 ± 0.109	0.888	88.83	10.73
50	0.958 ± 0.047	0.699	69.93	30.07
75	0.818 ± 0.021	0.597	59.68	40.32
150	0.750 ± 0.037	0.547	54.72	45.28
300	0.537 ± 0.053	0.392	39.17	60.83

Table 5. Comparative quantitative cell cycle distribution of SiHa cells in control and taurolidine treatment

Cell Cycle Phase	Gating region	Control (%)	Taurolidine treatment (%)
G0/G1	P2	59.08	74.96
S	P4	4.36	13.88
G2/M	P3	0.00	7.16

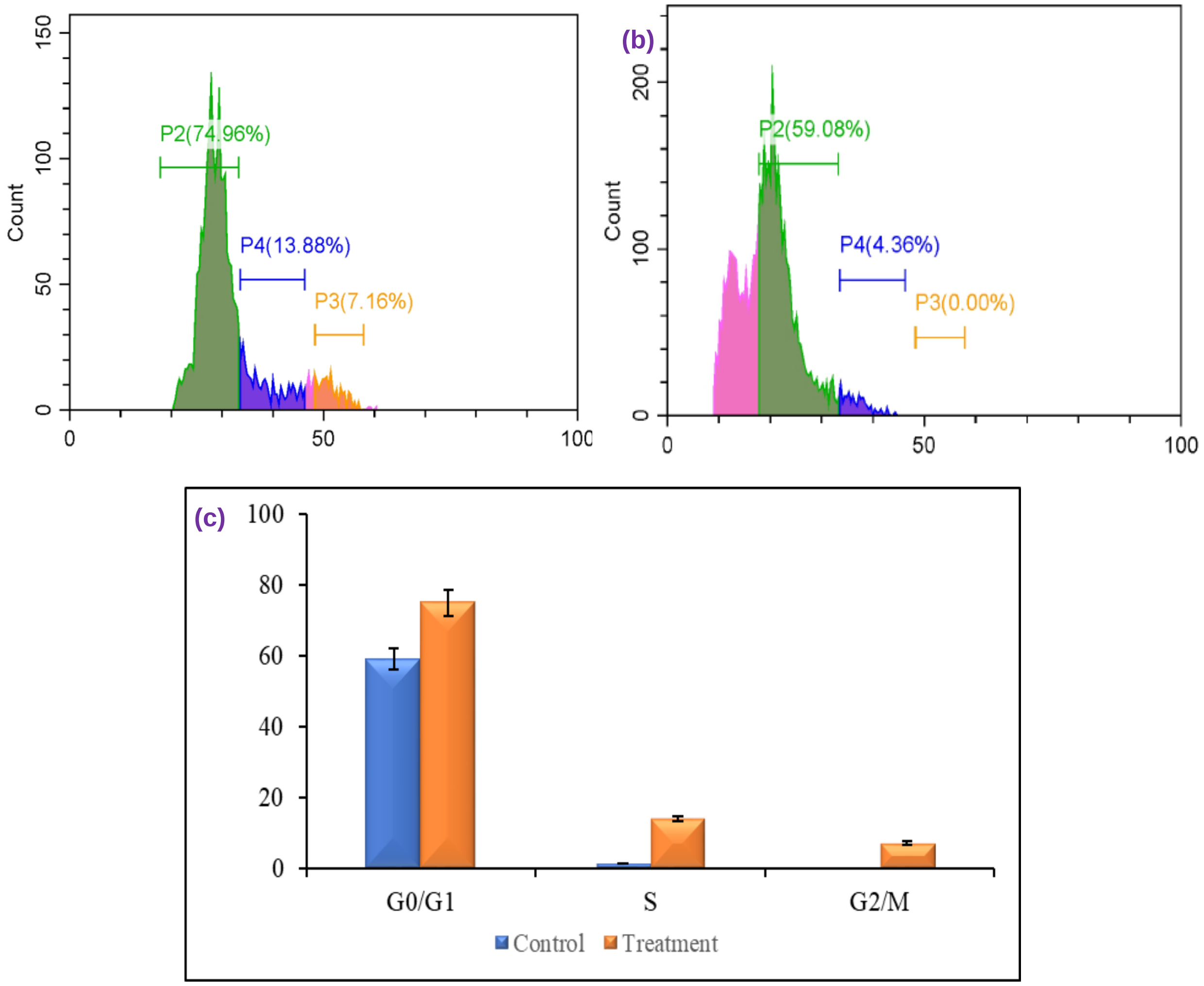

Figure 7. Effect of taurolidine on distribution of cervical cell carcinoma (SiHa) cells in diverse phases of cell cycle progression. The SiHa cells were induced with taurolidine at a 204.1 μM concentration for 24h followed by PI staining before flow cytometric examination. The concentration of DNA was quantified using PI fluorescence to measure the cell cycle phase distribution. Results are presented as monoparametric histograms: control (untreated cells) and SiHa cells treated with taurolidine for 24h.

These findings emphasize that taurolidine induces cell cycle halt in SiHa cells at G0/G1 phase, confirming its significant cell proliferation inhibitory characteristics against cervical cancer. Whereas the antiproliferative characteristics of taurolidine in cervical cancer cells by ha+lting the cell cycle in the G0/G1 phase leads to an increased percentage of cells in the sub-G1 phase, which enhances programmed cell death.

3.7. Acridine orange and ethidium bromide staining

The apoptotic characteristic of taurolidine against SiHa cells was measured using AO/EtBr dual staining. The cells with diffused and condensed chromatins were stained with green and orange hues, highlighting the viable and apoptotic cells [33-35]. The acridine orange (AO), ethidium bromide (EtBr), and combined AO/EtBr staining of control and taurolidine-treated cells are shown in Figure. 8. AO, a membrane-permeable fluorescent dye, binds to the nuclear DNA of active cells and emits green fluorescence. EtBr, an intercalating agent and impermeable fluorescent dye, binds to the DNA of apoptotic or necrotic cells, emitting red fluorescence. The cells treated with taurolidine (IC_{50} = 204.1 µM) showed a solid increase in the concentration of orange-green (apoptotic), bright red (necrotic), and dark orange (late apoptotic) cells in contrast to control cells.

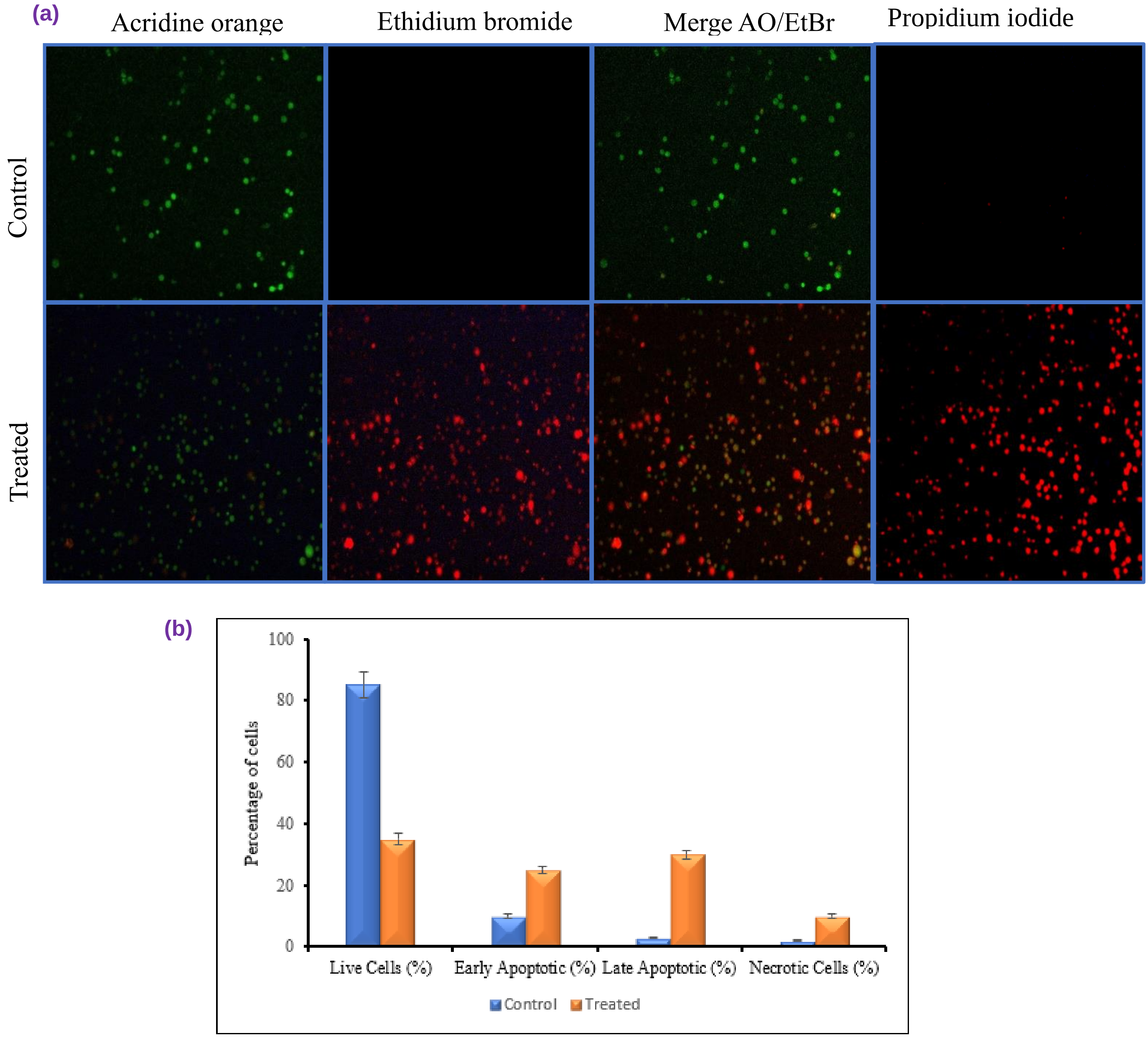

Figure 8. (a) The morphological characteristics of nuclei in SiHa cells, untreated and taurolidine-treated cells, are stained with propidium iodide (PI), exhibiting nuclear condensation and fragmentation in taurolidine-treated cells. Dual (Acridine orange/Ethidium bromide) staining ameliorates nuclear fragmentation, and morphological apoptotic features are observed in taurolidine-treated cells. **(b)** Quantitative apoptotic and necrotic percentage of cells in control and taurolidine-treated cells.

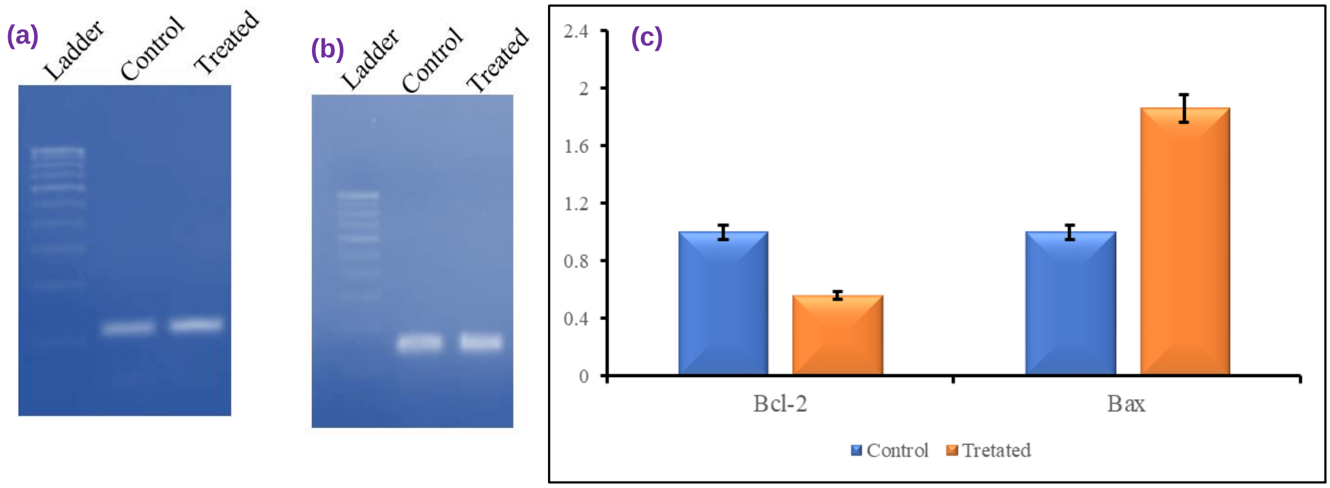

Figure 9. Quantitative RT-PCR measurement of (a) Bcl-2 and (b) Bax, (c) in control (untreated) and taurolidine-treated cells, the concentrations are shown as fold change as associated to control cells.

According to the findings, taurolidine induces morphological changes and triggers apoptosis and necrosis in cervical cancer cells.

3.8. Propidium iodide (PI) staining

Propidium iodide, a membrane-impermeable intercalating red fluorescent dye, binds to the nuclear DNA of apoptotic cells and emits red fluorescence. The characteristics of apoptosis, such as fragmentation and chromatin condensation, in taurolidine-induced SiHa cells were measured using PI staining. The propidium iodide staining of control and taurolidine-treated cells are shown in Figure. 6. The carcinoma cells treated with taurolidine at a concentration of 204.1 µM exhibit a solid increase in red fluorescence compared to control cells with uniform nuclear morphology. These findings demonstrate that taurolidine induces apoptosis by nuclear condensation and fragmentation in cervical cell carcinoma, confirming the antiproliferative activity of taurolidine.

3.9. Gene expression analysis

The m-RNA concentration of pro-apoptotic and anti-apoptotic proteins such as Bax and Bcl-2 in control and taurolidine-induced carcinoma cells were quantified using RT-PCR analysis. The Bcl-2 family of proteins regulates the homeostasis between cell survival and mortality attributed to pro and anti-apoptotic proteins. During apoptotic signaling, Bax integrated into the membrane of mitochondria, and released cytochrome-c into the cytosol, formed a complex with Apaf-1 and activates caspases [36, 37]. In this investigation, the expression stages of proteins Bcl-2 and Bax were measured in control and experimental groups shown in Figure. 9. The concentration of Bcl-2 was significantly reduced compared to control one, confirming the antagonist property of taurolidine against anti-apoptotic protein. In contrast, the concentration of Bax was notably increased compared to control, confirming the agonist characteristics of taurolidine against pro-apoptotic protein.

4. Conclusion

The structural, antiproliferative, and cytotoxic activity of taurolidine against cultured SiHa cells was analyzed using *in silico* and *in vitro* studies. In the Hirshfeld surface analysis, the fingerprint plot for O…H/H…O reveals the hydrogen bonding between the oxygen atom in sulfonyl groups and hydrogen atoms in the methylene groups, with bond distances of 2.341 and 2.806 Å. In molecular docking prediction, taurolidine forms three polar and nonpolar interactions with Bcl-2, exhibiting a binding affinity of -5.54 kcal/mol. In contrast, taurolidine forms three hydrophobic interactions with Bcl-XL, exhibiting a binding interaction of -6.92 kcal/mol. The percentage of cell death increased in the presence of taurolidine against SiHa cells with an IC_{50} (half maximal inhibitory concentration) at 204.1 µM, which was confirmed with MTT assay. In flow cytometric analysis, after 24hrs of taurolidine administration, the population of cells increased in the G0/G1 phase with 74.96% compared to control with 59.08%, confirming that taurolidine induces cell cycle halt in G0/G1 phase. The fluorescence AO/EtBr and PI confirm the taurolidine-induced cell death in SiHa cells. The antagonist and agonist characteristics of taurolidine were confirmed by gene expression analysis of pro and anti-apoptotic proteins.

References

[1] M. Vu, J. Yu, O.A. Awolude, L. Chuang, Cervical cancer worldwide. Current problems in cancer, 42(5), (2018) 457-465. https://doi.org/10.1016/j.currproblcancer.2018.06.003

[2] F. Bray, M. Laversanne, H. Sung, J. Ferlay, R.L. Siegel, I. Soerjomataram, A. Jemal, Global

cancer statistics 2022: GLOBOCAN estimates of incidence and mortality worldwide for 36 cancers in 185 countries. CA: a cancer journal for clinicians, 74(3), (2024) 229-263. https://doi.org/10.3322/caac.21834

[3] A. Buskwofie, G. David-West, C.A. Clare, A review of cervical cancer: incidence and disparities. Journal of the National Medical Association, 112(2), (2020) 229-232. https://doi.org/10.1016/j.jnma.2020.03.002

[4] K.S. Tewari, K.S, Cervical cancer. New England Journal of Medicine, 392(1), (2025) 56-71. https://doi.org/10.1056/NEJMra2404457

[5] D. Ramachandran, T. Dork, Genomic risk factors for cervical cancer. Cancers, 13(20), (2021) 5137. https://doi.org/10.3390/cancers13205137

[6] C. Chargari, K. Peignaux, A. Escande, S. Renard, C. Lafond, A. Petit, D.L.C. Kee, C. Durdux, C. Haie-Méder, Radiotherapy of cervical cancer. Cancer/Radiotherapie, 26(1-2), (2022) 298-308. https://doi.org/10.1016/j.canrad.2021.11.009

[7] A.S. Doghish, M.A. Ali, S.S. Elyan, M.A. Elrebehy, H.H. Mohamed, R.M. Mansour, A. Elgohary, A. Ghanem, A.H. Faraag, N.M. Abdelmaksoud, H.A.M. Moustafa, miRNAs role in cervical cancer pathogenesis and targeted therapy: Signaling pathways interplay. Pathology-Research and Practice, 244, (2023) 154386. https://doi.org/10.1016/j.prp.2023.154386

[8] P.M. Neary, P. Hallihan, J.H. Wang, R.W. Pfirrmann, D.J. Bouchier-Hayes, H.P. Redmond, The evolving role of taurolidine in cancer therapy. Annals of surgical oncology, 17, (2010) 1135-1143. https://doi.org/10.1245/s10434-009-0867-9

[9] E. Bobrich, C. Braumann, I. Opitz, C. Menenakos, G. Kristiansen, C.A. Jacobi, Influence of intraperitoneal application of taurolidine/heparin on expression of adhesion molecules and colon cancer in rats undergoing laparoscopy. Journal of Surgical Research, 137(1), (2007) 75-82. https://doi.org/10.1016/j.jss.2006.07.013

[10] R. Rodak, H. Kubota, H. Ishihara, H.P. Eugster, D. Könü, H. Möhler, Y. Yonekawa, K. Frei, Induction of reactive oxygen intermediates dependent programmed cell death in human malignant ex vivo glioma cells and inhibition of the vascular endothelial growth factor production by taurolidine. Journal of neurosurgery, 102(6), (2005) 1055-1068. https://doi.org/10.3171/jns.2005.102.6.1055

[11] A.M. Chromik, A. Daigeler, D. Bulut, A. Flier, C. May, K. Harati, J. Roschinsky, D. Sülberg, P.R. Ritter, U. Mittelkötter, S.A. Hahn, Comparative analysis of cell death induction by Taurolidine in different malignant human cancer cell lines. Journal of Experimental & Clinical Cancer Research, 29, (2010) 1-16. https://doi.org/10.1186/1756-9966-29-21

[12] A. Mani, R. Elaiyaraja, Comprehensive Theoretical Insights on Spectroscopic Characterization, Solvent Effect (Polar and Nonpolar) in Electronic behavior, Topological Insights, and Molecular Docking Prediction of Taurolidine, Int. Res. J. Multidiscip. Technovation, 6(6), (2024) 54-70. https://doi.org/10.54392/irjmt2464

[13] C. Braumann, G. Winkler, P. Rogalla, C. Menenakos, C.A. Jacobi, Prevention of disease progression in a patient with a gastric cancer-re-recurrence. Outcome after intravenous treatment with the novel antineoplastic agent taurolidine. Report of a case. World journal of surgical oncology, 4, (2006) 1-6. https://doi.org/10.1186/1477-7819-4-34

[14] A. Daigeler, A.M. Chromik, A. Geisler, D. Bulut, C. Hilgert, A. Krieg, L. Klein-Hitpass, M. Lehnhardt, W. Uhl, U. Mittelkötter, Synergistic apoptotic effects of taurolidine and TRAIL on squamous carcinoma cells of the esophagus. International journal of oncology, 32(6), (2008) 1205-1220. https://doi.org/10.3892/ijo.32.6.1205

[15] L. Nici, B. Monfils, P. Calabresi, The effects of taurolidine, a novel antineoplastic agent, on human malignant mesothelioma. Clinical cancer research, 10(22), (2004) 7655-7661. https://doi.org/10.1158/1078-0432.CCR-0196-03

[16] Francesco Caruso, James W. Darnowski, Cristian Opazo, Alexander Goldberg, Nina Kishore, Elin S. Agoston, Miriam Rossi CCDC 729501: Experimental Crystal Structure Determination, 2016.

[17] P.R. Spackman, M.J. Turner, J.J. McKinnon, S.K. Wolff, D.J. Grimwood, D. Jayatilaka, M.A. Spackman, CrystalExplorer: a program for Hirshfeld surface analysis, visualization and quantitative analysis of molecular crystals. Journal of Applied Crystallography, 54(3), (2021) 1006–1011. https://doi.org/10.1107/S1600576721002910

[18] G.M. Morris, R. Huey, W. Lindstrom, M.F. Sanner, R.K. Belew, D.S. Goodsell, A.J. Olson, AutoDock4 and AutoDockTools4: Automated docking with selective receptor flexibility. Journal of computational chemistry, 30, (2009) 2785-2791. https://doi.org/10.1002/jcc.21256

[19] A.C. Wallace, R.A. Laskowski, J.M. Thornton, LIGPLOT: a program to generate schematic diagrams of protein–ligand interactions. Protein Engineering, 8, (1995) 127–134. https://doi.org/10.1093/protein/8.2.127

[20] W.L. DeLano, Pymol: an open-source molecular graphics tool. CCP4 Newsletter on protein Crystallography, 40(1), (2002) 82–92.

[21] T. Lu, F. Chen, Multiwfn: a multifunctional wavefunction analyser. Journal of computational chemistry, 33, (2012) 580-592. https://doi.org/10.1002/jcc.22885

[22] R.A. Laskowski, J. Jabłonska, L. Pravda, R.S. Varekova, J.M. Thornton, PDBsum: Structural summaries of PDB entries. Protein science, 27(1), (2018) 129-134. https://doi.org/10.1002/pro.3289

[23] G. Ramakrishnan, L. Lo Muzio, C.M. Elinos-

Baez, S. Jagan, T.A. Augustine, S. Kamaraj, P. Anandakumar, T. Devaki, Silymarin inhibited proliferation and induced apoptosis in hepatic cancer cells. Cell Proliferation, 42(2), (2009) 229-240. https://doi.org/10.1111/j.1365-2184.2008.00581.x

[24] K.C. Mohan, P. Gunasekaran, E. Varalakshmi, Y. Hara, S. Nagini, In vitro evaluation of the anticancer effect of lactoferrin and tea polyphenol combination on oral carcinoma cells. Cell Biology International, 31(6), (2007) 599-608. https://doi.org/10.1016/j.cellbi.2006.11.034

[25] A. Gohel, M.B. McCarthy, G. Gronowicz, Estrogen prevents glucocorticoid-induced apoptosis in osteoblasts in vivo and in vitro. Endocrinology, 140(11), (1999) 5339-5347. https://doi.org/10.1210/endo.140.11.7135

[26] P. Chomczynski, N. Sacchi, Single-step method of RNA isolation by acid guanidinium thiocyanate-phenol-chloroform extraction. Analytical biochemistry, 162(1), (1987) 156-159. https://doi.org/10.1016/0003-2697(87)90021-2

[27] W. Falek, R. Benali-Cherif, L. Golea, S. Samai, N. Benali-Cherif, E.E. Bendeif, I. Daoud, A structural comparative study of charge transfer compounds: Synthesis, crystal structure, IR, Raman-spectroscopy, DFT computation and hirshfeld surface analysis. Journal of Molecular Structure, 1192 (2019) 132-144, https://doi.org/10.1016/j.molstruc.2019.04.084

[28] I. Tankov, R. Yankova, Hirshfeld surface, DFT vibrational (FT-IR) and electronic (UV–vis) studies on 4-amino-1H-1, 2, 4-triazolium nitrate. Journal of Molecular Structure, 1179 (2019) 581-592, https://doi.org/10.1016/j.molstruc.2018.11.050

[29] J. Jenifer, A. Ram Kumar, S. Selvaraj, Computational study on the Structural and Spectroscopic Properties, Solvent Effects, Topological Insights, and Biological Activities of 2-[1-(2, 4-dichlorobenzyl)-1H-indazol-3-yl] Propan-2-ol as an Anticonvulsant Drug. International Research Journal of Multidisciplinary Technovation, 7(2) (2025) 198-222, https://doi.org/10.54392/irjmt25215

[30] A. Fatima, H. Arora, P. Bhattacharya, N. Siddiqui, K. M. Abualnaja, P. Garg, S. Javed, DFT, molecular docking, molecular dynamics simulation, MMGBSA calculation and Hirshfeld surface analysis of 5-sulfosalicylic acid. Journal of Molecular Structure, 1273 (2023) 134242, https://doi.org/10.1016/j.molstruc.2022.134242

[31] R. Arulraj, S. Sivakumar, S. Suresh, K. Anitha, Synthesis, vibrational spectra, DFT calculations, Hirshfeld surface analysis and molecular docking study of 3-chloro-3-methyl-2, 6-diphenylpiperidin-4-one. Spectrochimica Acta Part A: Molecular and Biomolecular Spectroscopy, 232 (2020) 118166, https://doi.org/10.1016/j.saa.2020.118166

[32] K. Preetha, E.B. Seena, P.K. Maniyampara, E. Manoj, M.P. Kurup, Synthesis, crystal structure, Hirshfeld surface analysis, DFT, molecular docking and in vitro antitumor studies of (2E)-2-[4-(diethylamino) benzylidene]-N-ethylhydrazinecarbothioamide. Journal of Molecular Structure, 1295 (2024) 136700, https://doi.org/10.1016/j.molstruc.2023.136700

[33] K. Kandhari, J.P. Mishra, R. Agarwal, R.P. Singh, Acacetin induces sustained ERK1/2 activation and RIP1-dependent necroptotic death in breast cancer cells. Toxicology and Applied Pharmacology, 462 (2023) 116409, https://doi.org/10.1016/j.taap.2023.116409

[34] A.R. George, S. Sajeev, K. Thangasamy, N. Geetha, Exploring the Anti-Proliferative Potential of Codariyocalyx motorius on HepG2 Cells via. Activation of Intrinsic Apoptotic Pathway. Pharmacological Research-Natural Products, 7 (2025) 100273, https://doi.org/10.1016/j.prenap.2025.100273

[35] P. Bhagriya, A. Shaikh, H. Roy, Picropodophyllotoxin alters EMT in neuroblastoma via inhibition of surface receptors IGF1R and ALK. Growth Hormone & IGF Research, 80, (2025) 101638, https://doi.org/10.1016/j.ghir.2025.101638

[36] H. Sultana, J. Kigawa, Y. Kanamori, H. Itamochi, T. Oishi, Sato S, S. Kamazawa, M. Ohwada, M. Suzuki, N. Terakawa. Chemosensitivity and p53-Bax pathway-mediated apoptosis in patients with uterine cervical cancer. Ann Oncol. 14(2) (2003) 214-9, https://doi.org/10.1093/annonc/mdg071

[37] Bharat B. Aggarwal, Nuclear factor-κB: The enemy within, Cancer Cell, 6(3) (2004) 203-208, https://doi.org/10.1016/j.ccr.2004.09.003

Authors Contribution Statement

A. Mani: Conceptualization, Formal analysis, Writing-original draft. R. Elaiyaraja: Methodology, Writing – review & editing, Investigation, Supervision. Both the authors read and approved the final version of the manuscript.

Funding

The authors declare that no funds, grants or any other support were received during the preparation of this manuscript.

Competing Interests

The authors declare that there are no conflicts of interest regarding the publication of this manuscript.

Data Availability

The data supporting the findings of this study can be obtained from the corresponding author upon reasonable request.

Has this article screened for similarity?

Yes

About the License